Atomic Structure and Dynamics of Epitaxial 2D Gold on Graphene at Elevated Temperatures

*Qu Chen[1], Kuang He, Alex W. Robertson, Angus I. Kirkland, Jamie H. Warner[1]**

[1]Department of Materials, University of Oxford, Parks Road, Oxford, OX1 3PH, United Kingdom

*Jamie.warner@materials.ox.ac.uk;

Abstract

The atomic structure and dynamics of gold on graphene is studied at temperatures up to 800°C using an *in-situ* heating holder within an aberration corrected transmission electron microscope. At this high temperature, individual gold atoms and nanoclusters are mobile across the surface of graphene. We capture dynamics of gold nanoclusters attaching to defect sites in graphene and also migrating along edges of holes in graphene. Gold nanoclusters show crystallinity even though the temperature is above their predicted melting points. Gold nanoclusters anchored to defect sites in graphene adopt epitaxial alignment with the graphene lattice, with discrete rotations between fixed orientations. We show that gold nanoclusters can be 2D with monolayer thickness and switch their crystal structure between two different phases. The melting of gold nanoparticles is reduced at these high temperatures by epitaxial interactions with graphene, which has important implications on the use of gold nanoclusters on graphene at elevated temperatures for applications such as catalysis.

KEYWORDS: Graphene, gold, nanoparticles, TEM, in-situ

Graphene is a promising candidate for heterogeneous catalyst support under harsh conditions, such as acid and alkaline environments, and elevated temperatures due to its large surface area, excellent mechanical properties, large conductivity, chemical inertness and thermal stability.[1–4] Various types of graphene supported catalytic metal/alloy/oxide have been explored in recent years, such as Pd,[5] Pt,[6] Au,[1,3,4,7] TiO_2,[8] MnO_2,[9] and RuCu,[10] providing versatile applications such as fuel cells and water treatment. Gold particles are of high catalytic performance in certain areas, including automobile exhaust cleanup and biomedical applications.[11,12]

The morphology of gold nanoparticles strongly affects its catalytic behaviour. The structural form of gold nanoparticles can vary in different conditions, from face centered cubic (FCC) to multiply twinned decahedral or icosahedral.[13,14] A quantitative phase map of gold nanoparticles based on first principles calculations has been established by Barnard *et al*, with the consideration of temperature and the nanoparticle diameter.[15] For a supported catalytic system, the morphology of the nanoparticles is also determined by the interaction between the particle and the substrate, in addition to the balance between the surface energy and internal strain,[16] leading to gold crystals with unique morphologies. Gold with a planar structure has been formed on the surface of graphene by Sasaki *et al*.[17] Both theoretical and experimental studies have been conducted to investigate the bonding between metals and graphene sheets.[18–21] Metal nanoparticles including gold are more likely to attach to the defective areas within graphene such as vacancies, dopants, and also the surface hydrocarbon contaminants, rather than have direct contact with the pristine graphene lattice regions.[1,22–25] The non-hexagonal rings and amorphous carbon have higher chemical reactivity and offer anchor sites to stabilize the metal particles, preventing them from migrating around on the surface. The anchor effect is especially essential to catalysts made from noble metals, enabling smaller particles to be better dispersed and remain stable during

catalytic reactions. The aggregation of metal catalyst nanoparticles into larger clusters is one of the main aspects behind loss of catalytic efficiency during cycled catalytic testing. Understanding the catalyst-substrate interactions at high temperatures is essential for knowing the mechanisms of agglomeration and can help develop new ways to sustain isolated nanoparticle catalysts.

Here we have observed a structure of epitaxial two-dimensional gold nanocrystals on graphene at elevated temperatures, which is an ideal structure for graphene supported catalyst system as it maximizes the reactive sites for catalytic reactions as every single gold atom is at surface. The gold nanoparticles showing highly crystalline phases at elevated temperature to 800°C, which is way above its melting point according to the depression of the melting points of nanoparticles in comparison with the bulk crystal.[26] Desirable stability of the gold crystals is achieved due to the anchoring effect generated from gold dopants within the graphene lattice, which is introduced via releasing gold atoms from the gold nanoparticles by electron beam radiation in aberration corrected transmission electron microscope (AC-TEM). Melting and crystallization processes have been captured with atomic resolution, which provides the opportunity for a deep analysis for the relationship between orientations of graphene and gold nanocrystals. This knowledge is essential for understanding how gold nanocrystals interact with monolayer graphene, as well as offers important data for targeted and efficient design of metal/graphene catalytic systems.

Results and Discussion

Gold nanoparticles with average diameter of 1.5 nm on graphene (histogram in Figure 1b) were produced by thermal evaporation with deposition rate carefully controlled at 0.1 nm/min (Figure

S1 in Supporting Information compares the gold nanoparticle distributions for two durations of evaporation). Figure 1a demonstrates the distribution of gold nanoparticles, as well as the corresponding electron diffraction pattern, which both graphene and gold lattice. Energy Dispersive X-ray spectroscopy (EDX) shows significant peaks for gold, and a strong peak for silicon that likely comes from the silicon nitride support membrane within the heating chip. The gold particles are located only on the amorphous hydrocarbon surface contaminates and not on the pristine area, which agrees will with the previous results.[23]

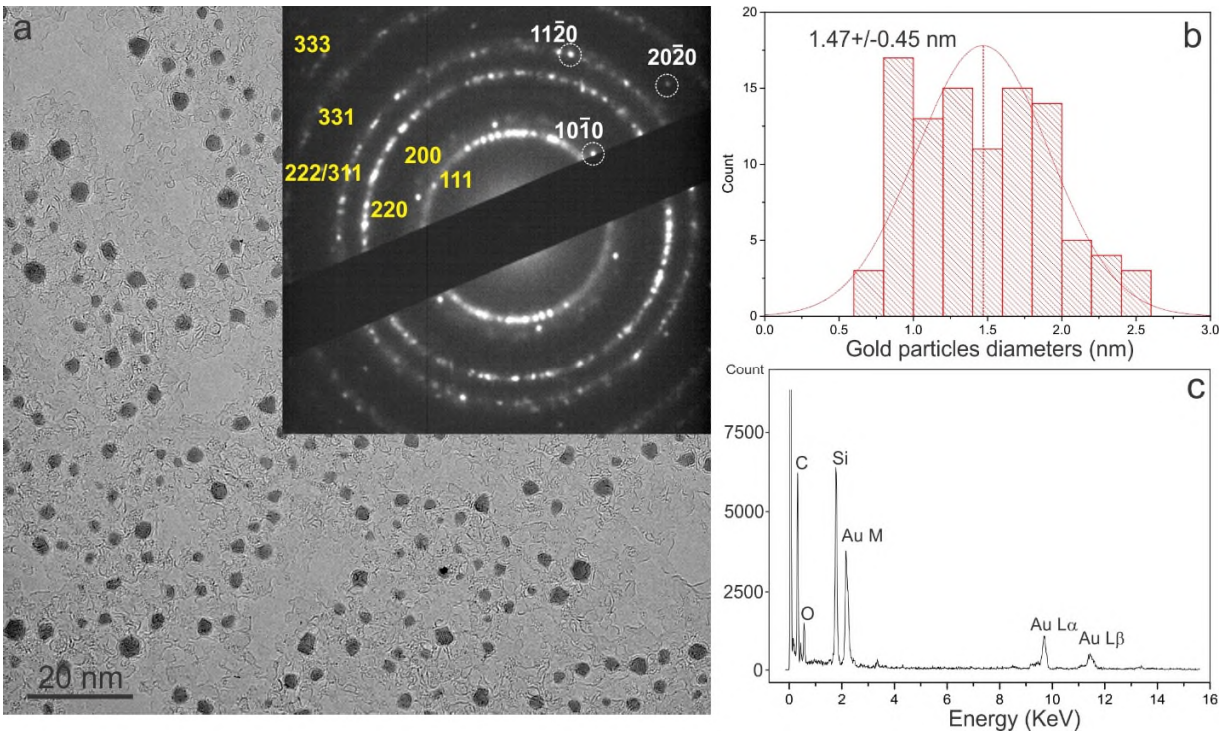

Figure 1 Distribution of gold particles deposited on graphene. a) Low magnification AC-TEM image, with the inset of its diffraction pattern (indices of crystal planes for graphene and gold are in while and yellow respectively). b) Histogram for the diameters of 100 gold particles. c) Corresponding EDX spectrum from 0 to 16 keV.

During the in-situ heating process, amorphous hydrocarbons crystallize under electron beam irradiation, forming a polycrystalline film on the top of the monolayer graphene, as shown in

Figure 2a. Graphene shells also form around the gold nanoparticles, indicated by the yellow arrows (see Figure S2 in Supporting Information for more core-shell structures). The graphene shells are robust at high temperature and under the electron beam, preventing gold nanoparticles from melting and migrating across the surface. However, small atomic clusters of gold without shells are observed in the multilayer region, highlighted in white dashed boxes in Figure 2a, and some molten gold clusters are found on the amorphous carbon regions (Figure 2b) and defective graphene region (Figure 2c). These atoms may have escaped from the larger gold clusters before the graphene shells fully encapsulate them.

It is also possible for the gold atoms to be embedded into graphene as substitutional dopants (Figure 2d). These small gold clusters are potential anchor sites for pinning gold nanocrystals that are freely migrating across the graphene surface. Figure 2e shows a gold array (highlighted in yellow box) with lattice contrast visible attaching to a graphene edge. Such a small gold cluster are expected to be molten at 800 °C due to the melting-point depression, as explained in Supporting Information S3. As labelled in the inset, the direction of one orientation of the gold atoms array (orange arrow) is parallel to one of the armchair direction of the surrounding graphene lattice, referring to a specific interaction between the graphene and gold crystalline phase.

Figure 3 shows a partially crystalline gold nanoparticle at the edge of a graphene hole. The size of the graphene hole is stable during the imaging period, and it can be observed that half of the gold particle is on the surface of the graphene region, and the other half is free-standing, with no support substrate underneath. The graphene-supported region of the gold particle is crystalline, with the contrast spots arranging in order, while the free-standing part shows blurring, indicating molten state. During the migration, some gold atoms break away from the gold cluster, forming ordered ultra-small clusters with two periodic type, one is square (Figure 3c, d and h), the other one is

triangular (Figure 3f, g), which has the same periodic structure with the gold cluster but with different orientations (highlighted in yellow dots and lines in Figure 3f). The distance between each two adjacent gold atoms is around 0.28 nm for both cases, corresponding to the distance between atoms in monolayer {100} and {111} planes of gold crystal. The partially crystalline gold cluster was finally broke apart by the electron beam, leaving ordered ultra-small clusters with the two types of ordered phases along the graphene edge (see Figure S4 in Supporting Information). This partially crystalline gold nanoparticles further prove the capability of graphene in crystallizing gold nanoparticles.

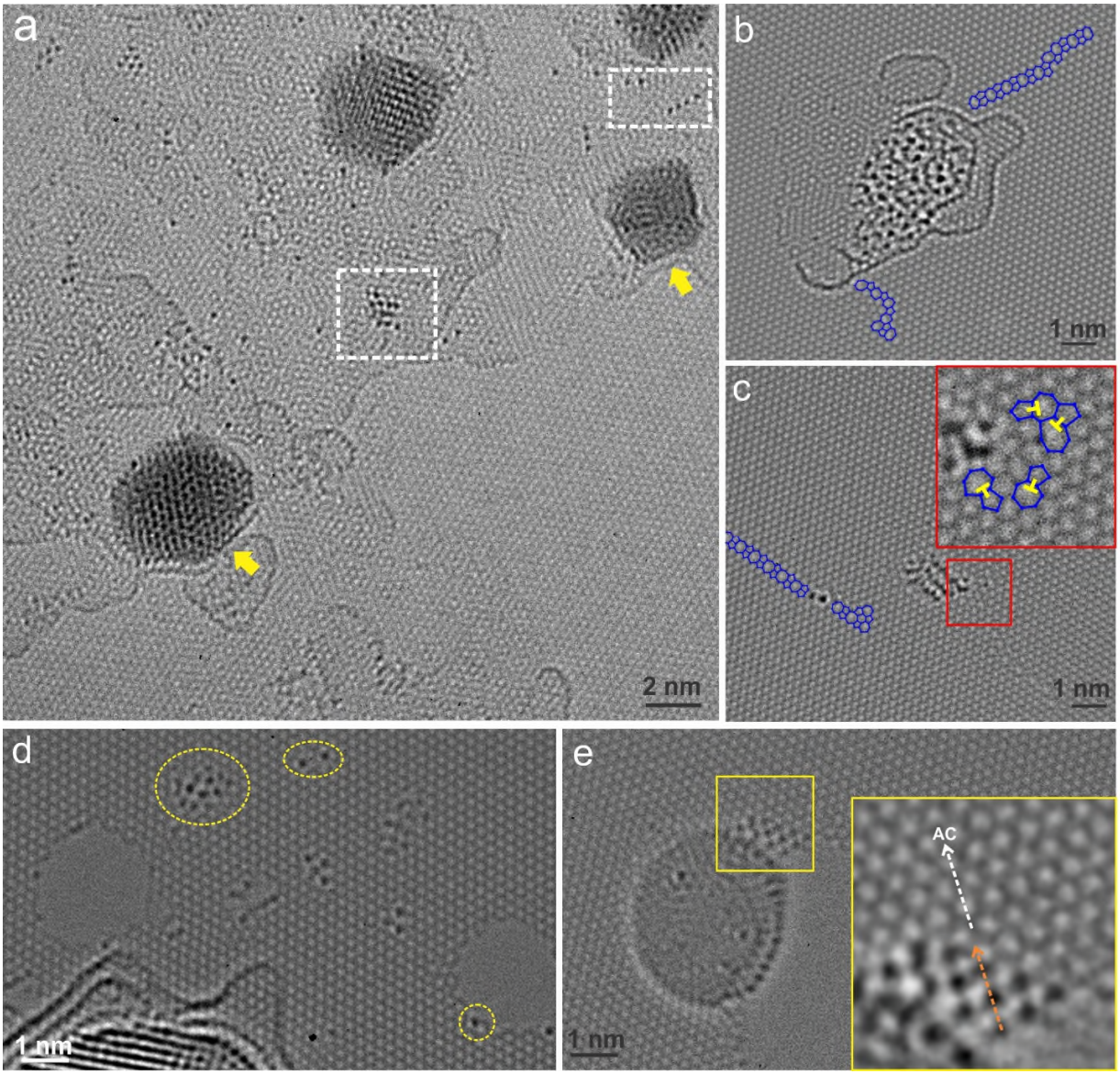

Figure 2 AC-TEM image of gold particles at 800 °C. a) Gold nanocrystals at polycrystalline graphene and amorphous regions, with some small gold clusters highlighted in white boxes. b) A disordered gold crystal at an amorphous region, with line defects nearby. c) A small gold cluster at defective region of monolayer graphene. e) Gold atoms settling in monolayer graphene lattice or at graphene edges after escaping from gold crystals. f) A small gold cluster with ordered phase attaching to a graphene edge.

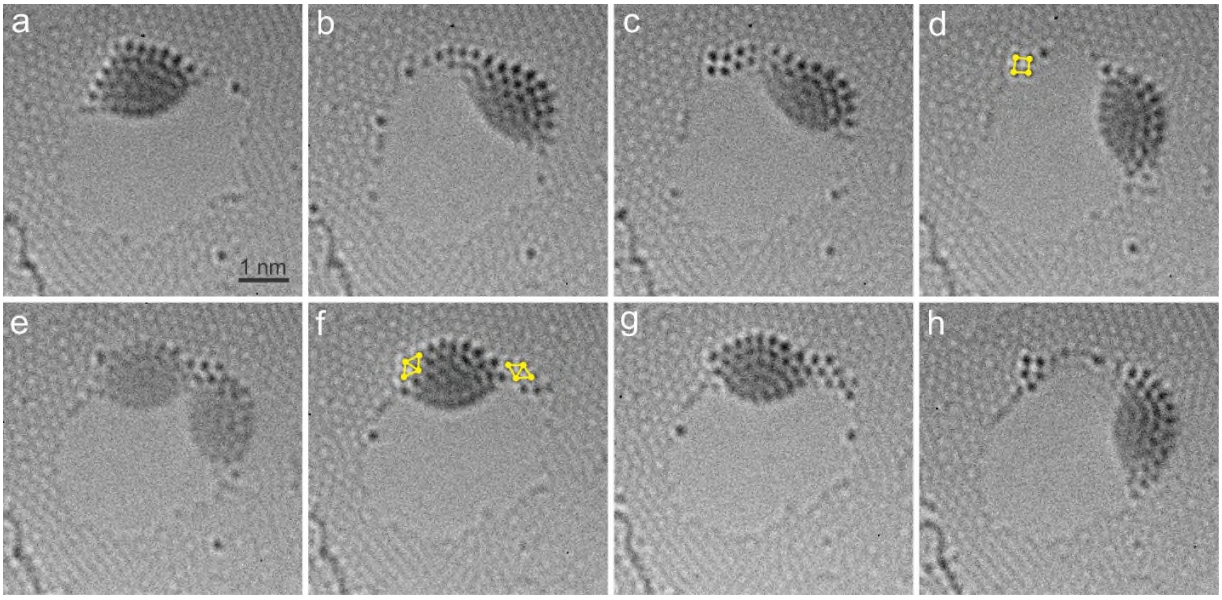

Figure 3 (a)-(h) AC-TEM images showing the dynamics of a gold nanoparticles moving around the edge of a hole in graphene. Time between each frame: ~10 s.

The TEM images of gold clusters attached to the edge of graphene show that the interactions between the gold and graphene result in crystalline ordering of the gold atoms in directions epitaxially matching the graphene lattice directions. We found that gold clusters without graphene shells were also mobile across the surface of graphene, only sticking to edges of holes or defect clusters. These sites provide anchoring points that temporarily slow down the gold cluster movement. In Figure 4 we examine two examples of the dynamics and structure of typical gold cluster that is moving around a hole edge and then jumps across to a defect site in the graphene lattice. In both cases, the gold cluster adheres to the graphene edge in the first place (Figure 4a and 4d), it then hops onto the defective area (highlighted by red circle in 4a and 4d) nearby, fixing itself onto the position. The image sequence shows that there is a pinning effect with the small defect site acting as anchoring point. The defect contains gold substitutional dopants before the larger cluster migrates to it and sticks, and therefore strong Au-Au bonds may form between the atoms in the gold defect and the upper gold crystal, preventing it from randomly migrating around.

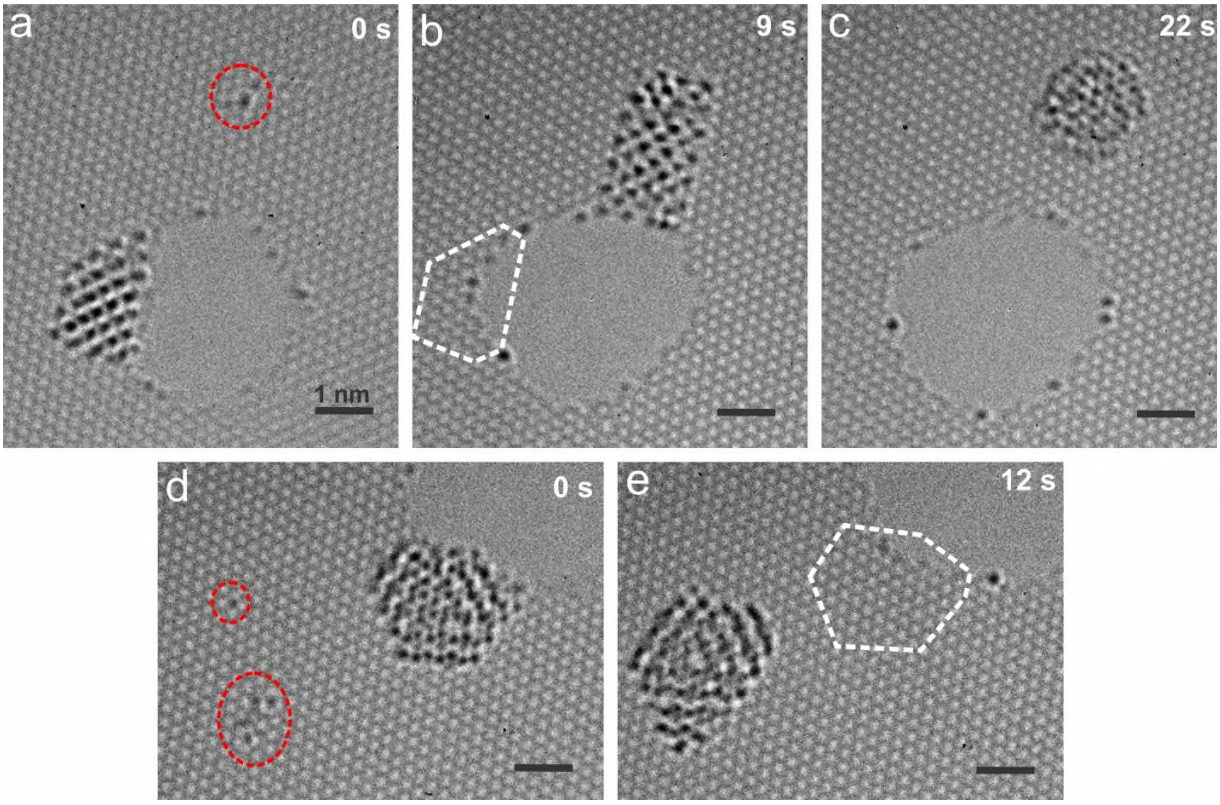

Figure 4 AC-TEM images showing gold clusters moving from the edge of a graphene hole to a defective site (highlighted by red dash circles).(a)-(c) Example 1, (d)-(e) Example 2. White dash boxes in b) and e) indicates the position of the gold crystal in the previous frame.

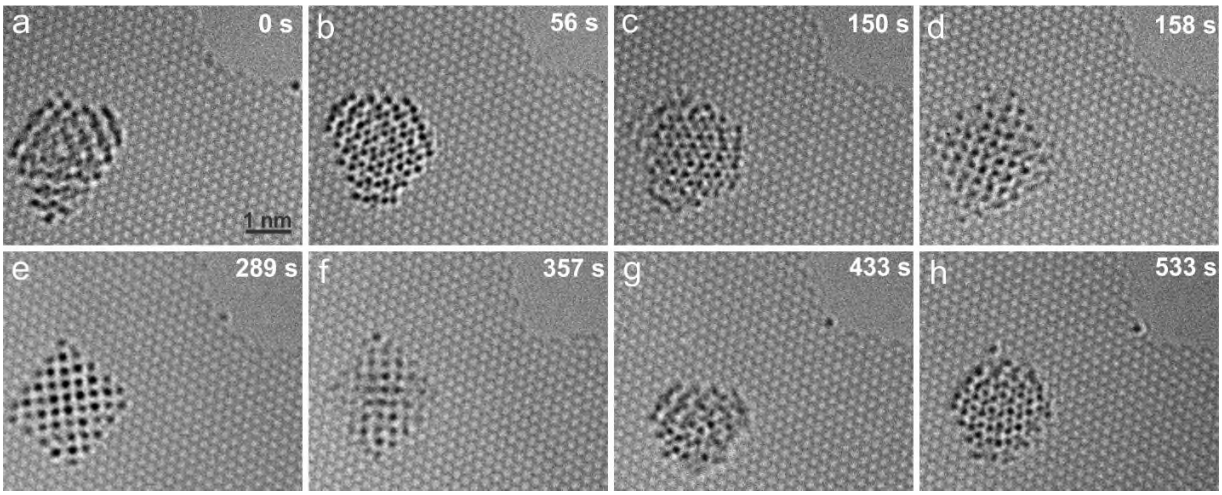

Figure 5 (a)-(h) Time series of AC-TEM images showing the dynamics of a gold cluster anchored to a defect site in graphene over a 9 minute period. a) The same gold cluster as the one shown in Figure 4e. b-h) Structural reconstructions of the gold cluster between the two crystalline phases: square and hexagonal.

Once the gold cluster is anchored, it undergoes several structural rearrangements. During the reconstruction process, the gold cluster forms unambiguous structures, with each contrast spot being isolated, as 5b, e and h, while the frames between them possess vague configurations, as 5a, c, d and f and g. The former structures indicate highly ordered crystalline phases, whereas the latter ones represent amorphous and molten states during transitions between the stable crystalline phases. A detailed phase transition of a gold crystal from square to hexagonal form is presented in Figure S4 in Supporting Information. This observation shows that the epitaxial interactions between the highly crystalline graphene and the gold particles cause crystallization above its melting point. Figure S5 in Supporting Information provides one more example to support this observation.

The number of contrast spots in Figure 5b, 5e and 5h may provide an insight into the loss or gain of gold atoms during the transformation process. Due to the slightly blurred areas at the edge of the crystal, only estimation of the number of atoms can be obtained. The hexagonal crystal in Figure 5b consists of about 87 contrast spots, 74% more than the square crystal shown in Figure 5e. When the crystal restructures to the hexagonal phase (Figure 5h), the number of contrast spots goes back to around 80. It is unlikely that more than 30 gold atoms are lost during the first phase transition, and then a similar number of atoms came back within the second transition. Furthermore, the nearby graphene hole remains relatively free from gold atoms during the whole period and if gold atoms were being released from the cluster we would expect a significant number to attach to this edge. Therefore, a plausible explanation is that no significant atom loss occurred during the

process, but rather at some positions within the square crystal (5e), one contrast spot corresponds to more than one gold atom in the projected direction of viewing in AC-TEM.

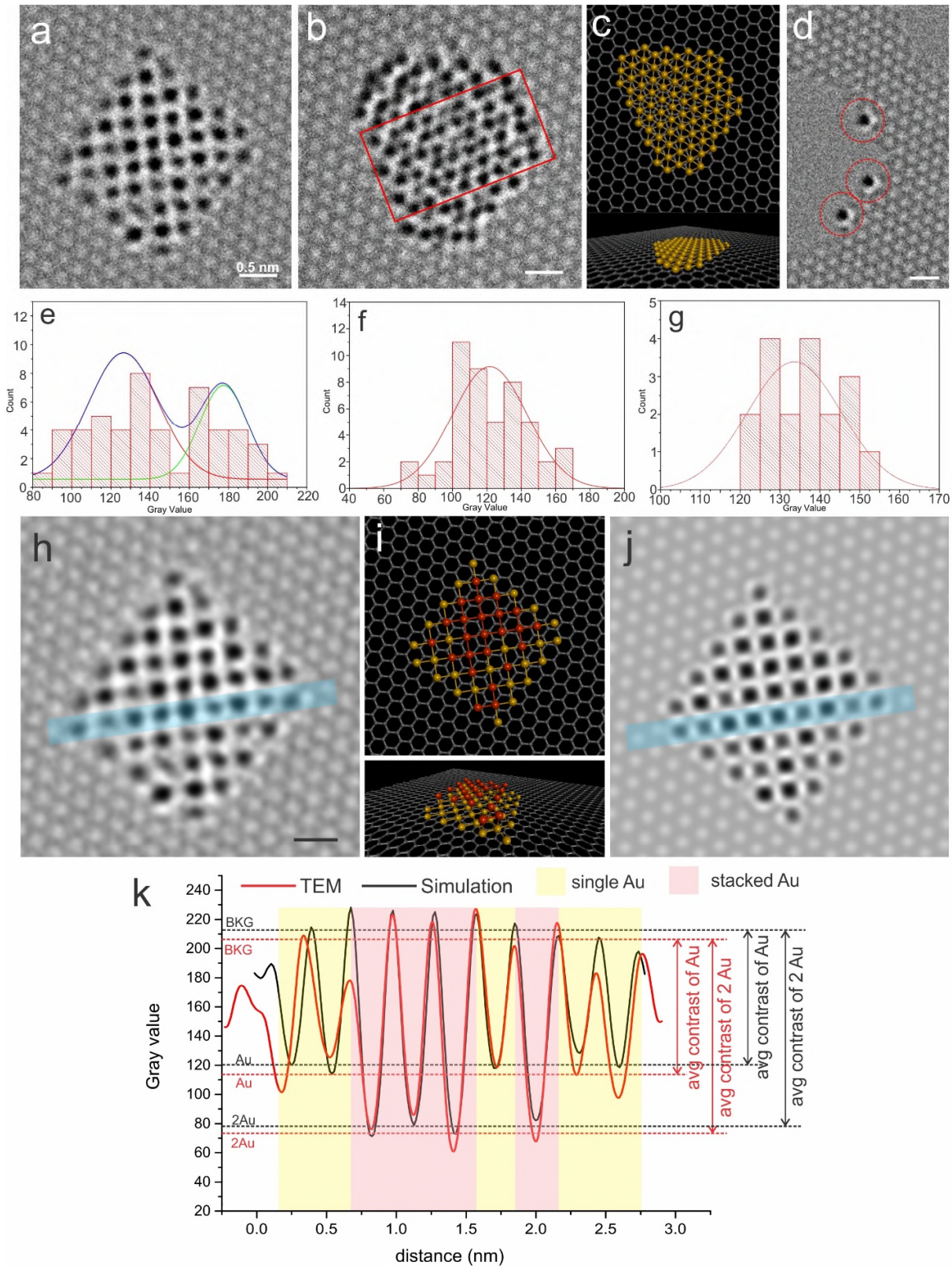
a
0.5 nm
b
c
d
e
Count
Gray Value
f
Count
Gray Value
g
Count
Gray Value
h
i
j
k
TEM
Simulation
single Au
stacked Au
BKG
BKG
Au
Au
2Au
2Au
Gray value
distance (nm)
avg contrast of Au
avg contrast of 2 Au
avg contrast of Au
avg contrast of 2 Au

Figure 6 Analysis of gold cluster thickness. a) AC-TEM image of the square gold crystalline phase (same with Figure 3e). b) AC-TEM image of the hexagonal gold crystalline phase (same with Figure 3a). c) Top and perspective views of the atomic model of b). d) Isolated gold atoms adhering to the graphene edge. e) Histogram of intensity values measured from the 50 contrast spots within the gold crystal shown in a). f) Histogram of intensity values of the 50 gold atoms contained in the red box shown in b). g) Histogram of intensity values of 20 isolated gold atoms at graphene edges. h) Smoothed AC-TEM image of the squared gold crystal. i) Top and perspective view of the atomic model of the squared crystal, with golden balls representing the first-layer gold atoms, and red balls representing the second layer. j) Multislice image simulation based on the model in i). k) Box-average intensity profiles of gold contrast spots for the blue areas in h) and j).

The partial-double-layer feature of the square shaped gold crystal is further confirmed by the examination of the relative contrast for each lattice site in the TEM image. The contrast intensity for a single atomic column within a gold crystal lattice image is determined by three factors, the number of the atoms along the projected direction, the stability during the 2 s acquisition time, and the error caused by the noise level of the AC-TEM image. Due to the heavy nature of gold atoms and reasonable stability of the gold crystal, the number of gold atoms in z direction dominates the intensity value of a contrast spot. Figure 6e shows two distinct Gaussian distributions for the values of contrast associated with a single atomic column within the square crystal. The peak positions of the fitted Gaussian curves for the left side are ~125, and the right side ~175. The two Gaussian distributions are attributed to atomic columns having either one or two gold atoms within the square gold cluster. The contrast values of atomic columns for the hexagonal crystalline phase are shown in Figure 6f, and show only one Gaussian curve is needed to fit the distribution. The peak value of the Gaussian curve is ~122, similar to that for the single atomic column value of the square gold cluster in Figure 6e, indicating this is only one atom thick. To further confirm the single and double atom stacking features of the two gold crystals, 20 isolated gold atoms along graphene

edges are carefully selected with sufficient stability during the 2 s exposure time (details on the selection is described in Figure S6 in Supporting Information) to obtain a typical contrast value for single gold atoms, as shown in Figure 6g. Figure 6d shows an example of three selected gold atoms at graphene edge. The peak position of the fitted Gaussian curve in figure 6g gives a contrast value of the single gold atoms as ~132. All three images in figure 6a, 6b, 6d have been adjusted so that the contrast value of the carbon lattice is near identical, meaning the analysis of the gold atom contrast values are consistent across all images. These results confirm the monolayer feature of the hexagonal crystal, the contrast spots with smaller intensity values are due to a certain amount of instability within the exposure time. For the case of the square gold crystal, both single- and double-layer areas exist, as suggested by the atomic model in Figure 6i, vertically stacking of two gold atoms occurred at 24 sites, leaving the rest of the 26 sites as monolayer gold atoms. To further investigate the validity of the atomic model, we compare the experimental TEM image of the square gold cluster with a multislice image simulation (Figure 6j) based on the relative atomic model, where the defocus is set to match the TEM imaging conditions. The brightness and contrast of the simulated image has been adjusted to make the relative contrast of carbon atoms in the graphene lattice matched to the carbon atoms in the TEM image and therefore act as the reference value for the gold atom intensity (the intensity profiles for carbon atoms are in Figure S7 in Supporting Information). Figure 6k shows the intensity profiles for the contrast spots within the blue box in 6h and 6j, and the experimental and theoretical results agree well. With this atomic model, the total gold atoms within the square crystal is 74, in error within +/- 5 atoms due to the influence of the noise level. Losing around 10 gold atoms during the first reconstruction is far more reasonable than 35, and it also matches the number of atoms after the second reconstruction, which is counted as 80 atoms.

When comparing the Fast Fourier Transform (FFT) patterns of the area with the two gold crystalline phases (Figure 7c and 7i) to the pristine graphene lattice (Figure 7b and 7h), the spots for gold and graphene can be easily separated. The corresponding d-spacing for each FFT spot of the gold crystals (see Figure S8 in Supporting Information for details) are obtained, based on the reference of the graphene lattice. With the consideration of the FCC structure of gold crystal, the incident beam direction (observation direction) for the case of the hexagonal crystalline phase has to be from one of the <111> crystal directions (taking $[\bar{1}11]$ in Figure 7d for an example), because of the regular triangular shape formed by every three adjacent contrast spots in the TEM image, as well as the regular hexagonal FFT pattern of the gold particle. The magnified image in Figure 7d shows the Miller Indices for all the FFT patterns of both the gold crystal (yellow) and graphene (white) with the incident beam direction of $[\bar{1}11]$ based on the ratios and included angles measured from the FFT pattern. Spots associated with the fractional lattice planes: 1/3{202}, 1/3{422} and 2/3{202}, occur in addition to the expected {202} reflections. These forbidden reflections generate from the incompleteness of the FCC crystal, as the hexagonal crystalline phase consists of only one layer of {111} plane, and at least three layers are needed to form a complete unit cell of FCC.[27] Thermal expansion of gold crystals should be taken into consideration when discussing the lattice constant at elevated temperature. A 0.9% of expansion of gold lattice has been observed in prior work at 785°C,[28] and therefore the lattice constant for a bulk gold crystal at 800°C should be about 4.11 Å. In the case of the hexagonal crystalline phase, the lattice constant calculated from the Miller Indices is about 3.4 Å, corresponding to a 17% contraction in comparison to the bulk gold crystal. This shrinkage is significantly larger than previous reports, where only 2% reduction of the lattice constant was observed within the 2 nm gold crystals.[29] The larger contraction may be caused by the single-atom-thickness of the crystal with smaller coordination number of 6 (for a

FCC crystal, the coordination number of each atom is 12 in bulk crystal). For the case of the square crystalline phase (Figure 7g-i), the observation direction is <001> (taking [001] for example), and a forbidden reflection {10} emerges also because of the ultrathin structure, as shown in Figure 7j. The lattice constant in this case is 4.08 Å, which means the thermal expansion is counteracting the shrinkage by its ultrathin nature.

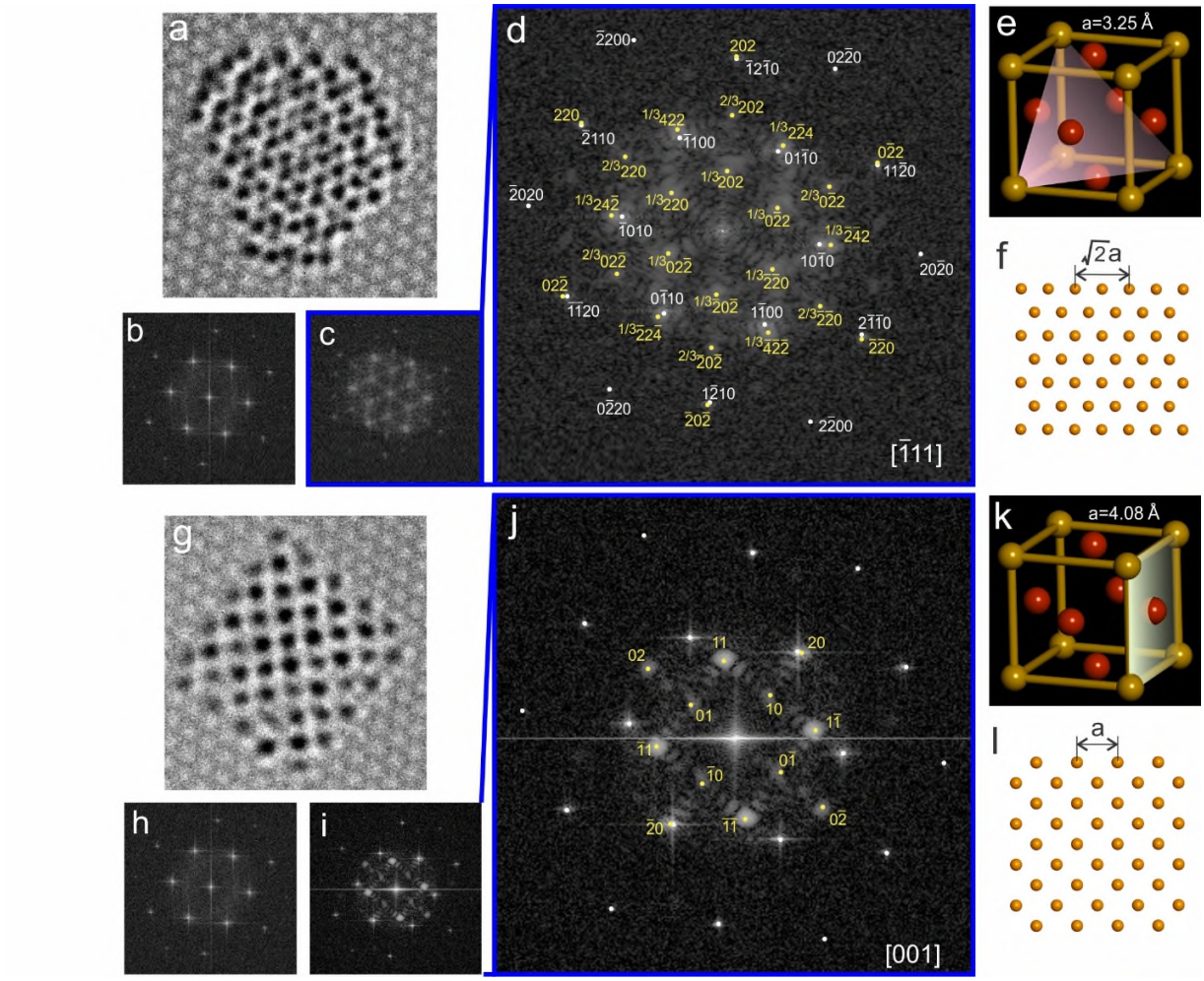

Figure 7 Crystallography of the two crystalline phases. a) The hexagonal gold crystal. b,c) Fast Fourier Transform (FFT) pattern of pristine graphene and graphene and gold crystal shown in a). d) Amplifying FFT pattern in c) with Miller Indices of each crystal planes. e) 3D atomic model for a face-centered cubic (FCC) unit cell for gold crystal, with a {111} plane highlighted by pink colour. f) Atomic model of {111} plane sliced from the FCC crystal. g) The square gold crystal. h, i) Fast Fourier Transform (FFT) pattern of

pristine graphene and graphene and gold crystal shown in e). j) Amplifying FFT pattern in i) with Miller Indices of each crystal planes. k) 3D atomic model for an FCC unit cell for gold crystal, with a {001} plane highlighted by green colour. l) Atomic model of {001} plane sliced from the FCC crystal.

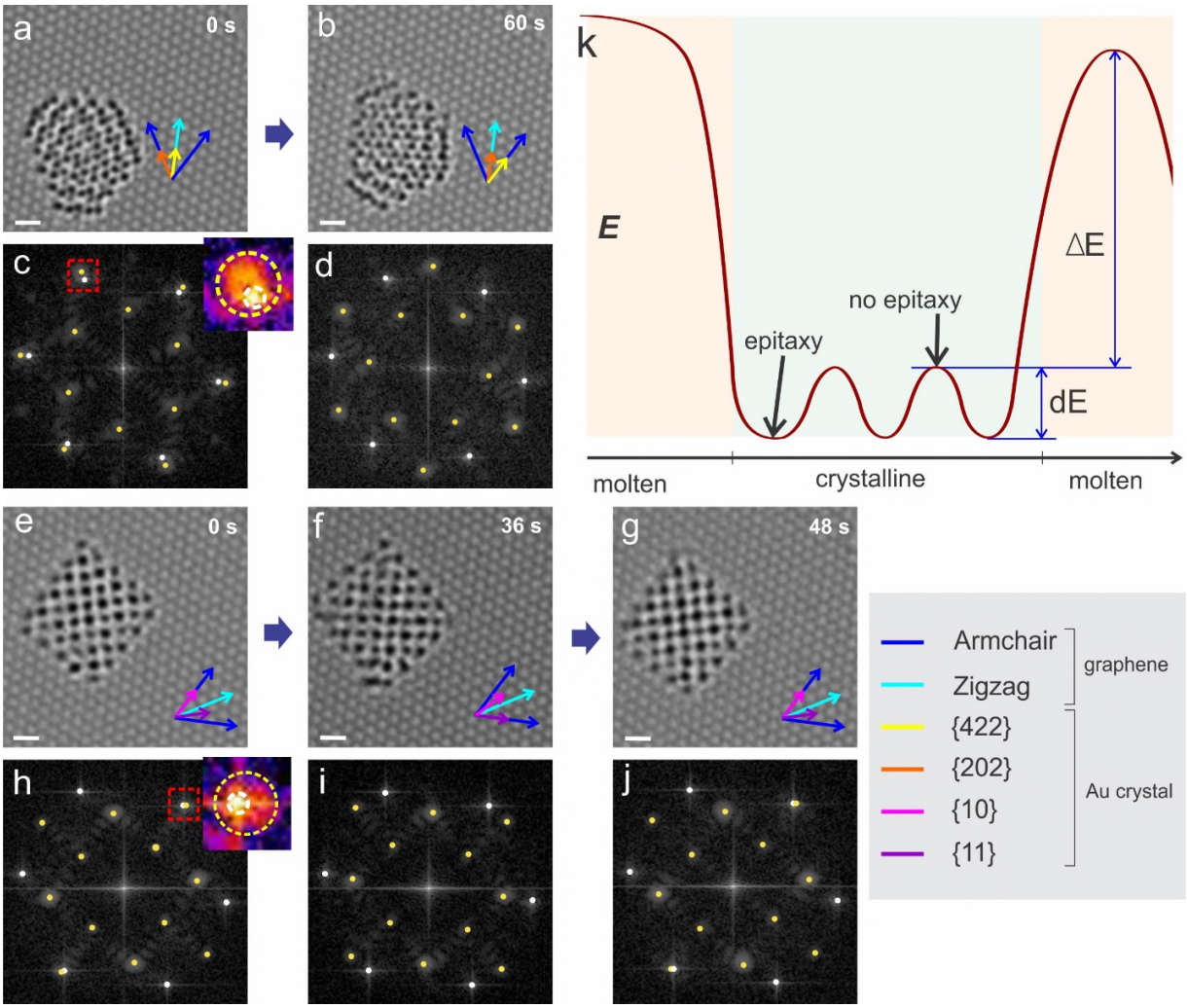

Figure 8 Epitaxial orientations of the gold crystalline phases on graphene. a,d) Two favored orientations for the hexagonal crystalline phase and corresponding FFT patterns, with the inset showing the detailed relationship between the 1/3{422} of gold crystal and {1010} of graphene. e-j) Transition between two epitaxial orientations of the squared gold crystal and corresponding FFT patterns, with the inset showing the detailed relationship between the {20} of gold crystal and {1010} of graphene. k) A schematic diagram of a hypothesis for energy barriers between each state.

When examining the relative orientations between the gold cluster and graphene based on their FFT patterns, we see a parallel relationship between the planes of the gold crystal and graphene. For the case of the hexagonal gold crystal, the first epitaxial situation is that the directions of the six spots representing for the d-spacing of $\frac{1}{3}\{422\}$ planes for gold coincide with the six spots for graphene $\{10\bar{1}0\}$ plane in reciprocal space, which means, in the real space, the {202} crystal plane of gold is parallel to the armchair direction of graphene, and {422} crystal plane is parallel to the zigzag direction, as shown in the arrows in Figure 8a. The d-spacing of $\frac{1}{3}\{422\}$ plane of gold and $\{10\bar{1}0\}$ plane of graphene show an approximately 6% mismatch, as shown in the inset of Figure 8c, where the centre of graphene and gold spots are not concentric. This orientation lasts 60 s, indicating some degree of stability. Figure 8b reveals the orientation of the same gold crystal after 60 s. It can be easily observed from both the TEM image and the corresponding FFT pattern (Figure 8d) that the gold crystal rotates 30° clockwise, which is the other epitaxial orientation, with the {422} crystal plane of gold parallel to the armchair direction of graphene, and {202} crystal plane parallel to the zigzag direction. This orientation also lasts nearly 60 s. The shape of the hexagonal gold crystal does not change much during the rotation. During the lifetime of this gold crystal, every time the highly crystalline phase with hexagonal structure appears, it shows either of the two epitaxial orientations. This indicates strong interaction between the gold crystal and graphene lattice, even though there may be some bonding between the anchoring defect and the 2D gold crystal to initially anchor it to the local region. Similar alignment between the gold and graphene lattice also occurs for the square gold crystalline phase, which is surprising given that cubic crystal structure does not have many epitaxial correlated atomic sites with the hexagonal crystal phase of graphene. We also find that the square crystalline phase oscillates between two preferred orientations, just like the case of the hexagonal crystalline phase. Figure 6e shows the

first epitaxial orientation, with {20} (or {10}) crystal plane parallel to one of armchair directions and the zigzag direction that is vertical to the armchair direction, due to the orthogonality of each plane in {20} group. After 36 s, the second epitaxial orientation appears, with the {11} crystal plane parallel to one armchair and one zigzag direction (Figure 8f and 8i). In this case, the square gold crystal rotates 15° clock wise. The gold crystal then rotates 15° anti-clockwise to the original epitaxial orientation in 12 s (Figure 8g and 8j).

Our observations of rotation indicates that the crystalline phases are more energetically favourable than the molten states when on clean graphene surface, and energy is required for the transitions between the two crystalline phases (square and hexagonal). When the gold is in its crystalline phases, matching graphene lattice directions are always found and indicate these are the low energy states. Energy is required to rotate between different graphene lattice directions of fixed stability. A schematic illustration in Figure 8k shows the possible energy variations between each crystallographic state. This indicates that it is the interactions between the graphene and gold lattice that is preventing the gold cluster from being in a molten state and instead adopting a high degree of crystalline order. This behaviour is not seen for gold clusters sitting on the amorphous carbon or on highly defective regions of monolayer carbon that have lost the periodic hexagonal lattice structure, further supporting the notion that epitaxial interactions drive the crystallization of gold.

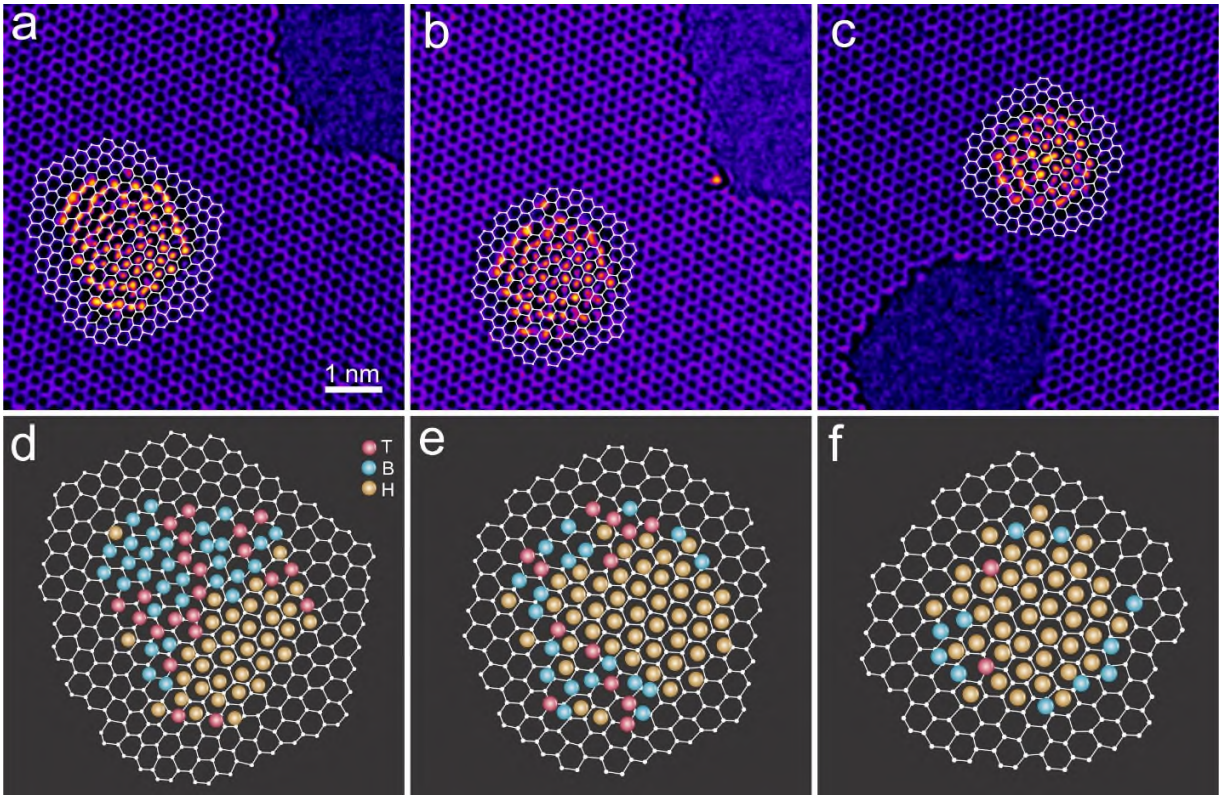

Figure 9 The relative positions gold atoms within the crystalline phases with respect to the graphene lattice structure. a-c) AC-TEM images with false colour showing the hexagonal crystalline phase of gold clusters, with underneath graphene lattice generated using a continuation of the surrounding area. d-f) Atomic models indicating the three types of positions gold atoms can adopt with respect to the graphene lattice, where red spheres correspond to atop sites, blue spheres correspond to bridge sites, and golden spheres corresponding to hollow sites.

The graphene lattice underneath the gold crystal contributes little contrast to the image in this region. However, by reconstructing of the image by selecting the FFT pattern for graphene only can we see the difference between the vacuum area and the region underneath the crystal (see Figure S9 in Supporting Information). Although there must be a small defective site somewhere in the covered graphene area, it is quite small and therefore we can create an extension of the surrounding area into the region below the gold cluster by continuation of the hexagonal ring pattern, as shown in Figure 9a-c, where the graphene lattice structures have been highlighted by

white lines. It provides detailed information about how individual gold atoms within a crystal locate with respect to the carbon atoms in graphene. According to previous research, single gold adatoms can sit in three sites on the surface of graphene: top, bridge and hollow sites, and the former two sites are more energetically favourable than the hollow site based on the DFT calculations.[30] For isolated gold adatoms on a graphene surface, the binding energy for the three sites are 0.79 eV for top, 0.74 eV for bridge, and 0.52 eV for hollow.[30] At high temperature (i.e 800^{o}C) the thermal energy is sufficient to overcome the energy barrier between these three configurations and therefore individual gold atoms are mobile across the graphene surface and do not bind to any particular site in pristine areas for an appreciable amount of time to image by TEM. The behaviour of the gold atoms within a 2D crystal differs from isolated ones due to the bonding with other gold atoms in the cluster, stabilizing the cluster. Figure 9d-f records the position of each gold atom based on their corresponding TEM images, with the graphene lattice projected into the gold cluster region to examine the possible correlations between the gold atom site and carbon atom sites. We find that hollow sites are favoured by these gold atoms (represented by the golden balls) across the three images in Figure 9. Gold atoms in the top and bridge sites mostly occur at the edge areas of the crystalline phase, along with severe distortions. The coordination number of the gold atoms at the central area is 6, while for the edge atoms it is 3 to 5. Fewer bonding to nearest neighbours induces variations of the distances between them and the edge atoms were loosely bonded and easily escaped from a crystal.[31]

Conclusion

Our observations of crystalline phase transitions and local rotations between the epitaxial orientations, indicates that the crystalline phases are more energetically favourable than the molten

states when on clean graphene surfaces. Energy is required to transition between the two crystalline phases (square and hexagonal). When the gold is in its crystalline phases, epitaxial orientations matching graphene lattice directions are always found and indicate these are the low energy states. Energy is required to rotate between different graphene lattice directions of fixed stability. This indicates that it is the interactions between the graphene and gold lattice that is preventing the gold cluster from being in a molten state and instead adopting a high degree of crystalline order. This behaviour is not seen for gold clusters on the amorphous carbon contamination or highly defective regions of monolayer carbon, further supporting the notion that epitaxial interactions drive the crystallization of gold.

Observing the epitaxial interactions between gold clusters deposited onto graphene was hindered by the formation of a graphene shells around the preformed gold nanoparticles that sealed them up and prevented further transformations. However, there were sufficient free gold atoms and small gold clusters that were able to migrate across the surfaces and form crystalline phases that depended on the nature of the carbon structure below. Our results indicate that the amorphous carbon contamination on the surface of graphene is the major inhibiting factor for the formation of large scale 2D gold on graphene. One possible way that this could be overcome in future work is to heat graphene to high temperatures first to clean its surface and then deposit gold at elevated temperature on the clean surface. These results shed important light into the gold-carbon interactions that are important for a variety of catalyst reactions, where small gold clusters are attached to carbon supports of various kinds ranging from graphene to carbon black.

Experimental Methods

CVD Synthesis of Monolayer Graphene. Monolayer graphene samples were grown by the previously reported method with tungsten (1 cm^2) supported molten copper as catalyst. Hydrochloric acid was applied to copper (1 cm^2) during preparation to remove the oxidised layer.[32] With all the metal substrates and catalysts being placed into the quartz tube in the furnace, 80 sccm of hydrogen (25%) and 200 sccm of argon was applied to flush the system until it stabilised at 1090 °C for 30 min. 10 sccm methane (1%) was then added to the gas flow to start the growth of graphene for 90 min, followed by a secondary growth at 1060 °C for 30 min. The methane was immediately stopped once the secondary growth of graphene was done. The samples were subsequently removed from the heating zone of the tube and cooled in air to room temperature.

Transfer of Graphene. The CVD grown graphene samples were firstly spin-coated with a poly(methyl methacrylate) (PMMA) scaffold and then cured at 180 °C for 90 s. Electrochemical etching in sodium hydroxide solution (2M) was applied to remove tungsten substrate, with a copper foil serving as anode.[33] The copper was then etched away by chemical etching with ammonium persulfate (0.1M). The transparent graphene with PMMA scaffold was then rinsed in deionised water for several times, followed by transferring them onto prefabricated in-situ heating chips and drying in air for 3 hours. 15 minutes of bake at 180 °C was applied to the sample to reinforce the adhesion between graphene and the wafer. PMMA scaffold was removed by heating the sample at 350 °C for about 12 hours.

Sub-nanometre Gold Deposition. Thermal evaporator was used to deposit sub-nanometre gold onto the graphene TEM samples. The current was precisely controlled to provide an extremely slow deposition (0.1 nm/min). The deposition process was immediately ceased once the thickness reached 0.1 nm.

Transmission Electron Microscopy with an in-situ Heating Holder. AC-TEM was performed using Oxford's JEOL JEM-2200MCO Field-Emission Gun TEM at 80 kV accelerating voltage, as well as a CEOS imaging aberration corrector. TEM Data were recorded by a Gatan Ultrascan 4K × 4K CCD camera with 2 s acquisition times. High temperature experiments was conducted by using Si_3N_4 TEM grid designed for in situ Transmission Electron Microscopy in a heating holder (DENSsolutions single tilt 30° fitted with DENSsolutions High Temperature EM heater chip with a maximum operating temperature up to 800 °C). Several windows was produced by Zeiss NVision SEM: FIB prior to graphene transfer within the thin Si_3N_4 membrane on the heating holder, in order to avoid the contrast from the Si_3N_4 membrane.

Image Processing. Image J was used to process the AC-TEM images. A bandpass filter (between 100 and 1 pixels) and a Gaussian blur were carefully applied to minimize long range uneven illumination without affecting the interpretation of the original image. Multislice image simulations was accomplished using JEMS software with supercells created using Accelrys Discovery Studio Visualizer.

Reference

(1) Julkapli, N. M.; Bagheri, S. Graphene Supported Heterogeneous Catalysts: An Overview. *Int. J. Hydrogen Energy* **2015**, *40*, 948–979.

(2) Deng, D.; Novoselov, K. S.; Fu, Q.; Zheng, N.; Tian, Z.; Bao, X. Catalysis with Two-Dimensional Materials and Their Heterostructures. *Nat. Nanotechnol.* **2016**, *11*, 218–230.

(3) Yu, X.; Huo, Y.; Yang, J.; Chang, S.; Ma, Y.; Huang, W. Reduced Graphene Oxide Supported Au Nanoparticles as an Efficient Catalyst for Aerobic Oxidation of Benzyl

Alcohol. *Appl. Surf. Sci.* **2013**, *280*, 450–455.

(4) Choi, Y.; Gu, M.; Park, J.; Song, H. K.; Kim, B. S. Graphene Multilayer Supported Gold Nanoparticles for Efficient Electrocatalysts toward Methanol Oxidation. *Adv. Energy Mater.* **2012**, *2*, 1510–1518.

(5) Scheuermann, G. M.; Rumi, L.; Steurer, P.; Bannwarth, W.; Mülhaupt, R. Palladium Nanoparticles on Graphite Oxide and Its Functionalized Graphene Derivatives as Highly Active Catalysts for the Suzuki-Miyaura Coupling Reaction. *J. Am. Chem. Soc.* **2009**, *131*, 8262–8270.

(6) Layek, R. K.; Samanta, S.; Nandi, A. K. The Physical Properties of Sulfonated Graphene/poly(vinyl Alcohol) Composites. *Carbon N. Y.* **2012**, *50*, 815–827.

(7) Kumar, S.; Selvaraj, C.; Munichandraiah, N.; Scanlon, L. G. Gold Nanoparticles Anchored Reduced Graphene Oxide as Catalyst for Oxygen Electrode of Rechargeable Li–O_2 Cells. *RSC Adv.* **2013**, *3*, 21706-21714.

(8) Liang, Y.; Wang, H.; Casalongue, H. S.; Chen, Z.; Dai, H. TiO_2 Nanocrystals Grown on Graphene as Advanced Photocatalytic Hybrid Materials. *Nano Res.* **2010**, *3*, 701–705.

(9) Chen, S.; Zhu, J.; Wu, X.; Han, Q.; Wang, X. Graphene Oxide−MnO_2 Nanocomposites for Supercapacitors. *ACS Nano* **2010**, *4*, 2822–2830.

(10) Cao, N.; Hu, K.; Luo, W.; Cheng, G. RuCu Nanoparticles Supported on Graphene: A Highly Efficient Catalyst for Hydrolysis of Ammonia Borane. *J. Alloys Compd.* **2014**, *590*, 241–246.

(11) Campbell, C. T. The Active Site in Nanoparticle Gold Catalysis. *Science.* **2004**, *306*, 234–

235.

(12) Ralph A. Sperling, Pilar Rivera Gil, Feng Zhang, M. Z. and; Parak, W. J. Biological Applications of Gold Nanoparticles. *Chem. Soc. Rev.* **2008**, *37*, 1909–1930.

(13) Young, N. P.; van Huis, M. A.; Zandbergen, H. W.; Xu, H.; Kirkland, A. I. Transformations of Gold Nanoparticles Investigated Using Variable Temperature High-Resolution Transmission Electron Microscopy. *Ultramicroscopy* **2010**, *110*, 506–516.

(14) Marks, L. D. Experimental Studies of Small Particle Structures. *Rep. Prog. Phys.* **1994**, *57*, 603–649.

(15) Barnard, A. S.; Young, N. P.; Kirkland, A. I.; Van Huis, M. A.; Xu, H. Nanogold: A Quantitative Phase Map. *ACS Nano* **2009**, *3*, 1431–1436.

(16) Yacamán, M. J.; Ascencio, J. a.; Liu, H. B.; Gardea-Torresdey, J. Structure Shape and Stability of Nanometric Sized Particles. *J. Vac. Sci. Technol. B Microelectron. Nanom. Struct.* **2001**, *19*, 1091-1103.

(17) Sasaki, Y.; Kitaura, R.; Yamamoto, Y.; Arai, S.; Suzuki, S.; Miyata, Y.; Shinohara, H. Preparation and Observation of an Atomic Layer of Gold Formed on the Surface of Graphene. *Appl. Phys. Express* **2012**, *5*, 065103-1 – 065103-3.

(18) Amft, M.; Sanyal, B.; Eriksson, O.; Skorodumova, N. V. Small Gold Clusters on Graphene, Their Mobility and Clustering: A DFT Study. *J. Phys. Condens. Matter* **2011**, *23*, 205301, 1-10.

(19) Brito, W. H.; Miwa, R. H. Adsorption and Diffusion of Gold Adatoms on Graphene Nanoribbons: An Ab Initio Study. *Phys. Rev. B - Condens. Matter Mater. Phys.* **2010**, *82*,

1–7.

(20) Grantier, J.; Lazar, P.; Prucek, R.; Šafářová, K.; Zbořil, R. Interaction of Graphene with Noble Metals. *J. Phys. Chem. C,* **2012**, 116, 1–44.

(21) Pulido, A.; Boronat, M.; Corma, A. Theoretical Investigation of Gold Clusters Supported on Graphene Sheets. *New J. Chem.* **2011**, *35*, 2153–2161.

(22) Zan, R.; Bangert, U.; Ramasse, Q.; Novoselov, K. S. Interaction of Metals with Suspended Graphene Observed by Transmission Electron Microscopy. *J. Phys. Chem. Lett.* **2012**, *3*, 953–958.

(23) Zan, R.; Bangert, U.; Ramasse, Q.; Novoselov, K. S. Metal - Graphene Interaction Studied via Atomic Resolution Scanning. *Nano letters,* **2011**, *11*, 1087–1092.

(24) Li, S.; Guo, S.; Yang, H.; Gou, G.; Ren, R.; Li, J.; Dong, Z.; Jin, J.; Ma, J. Enhancing Catalytic Performance of Au Catalysts by Noncovalent Functionalized Graphene Using Functional Ionic Liquids. *J. Hazard. Mater.* **2014**, *270*, 11–17.

(25) Liu, W.; Sun, D.; Fu, J.; Yuan, R.; Li, Z. Assembly of Evenly Distributed Au Nanoparticles on Thiolated Reduced Graphene Oxide as an Active and Robust Catalyst for Hydrogenation of 4-Nitroarenes. *RSC Adv.* **2014**, *4*, 11003–11011.

(26) Pawlow, P. Z. "Über die Abhängigkeit des Schmelzpunktes von der Oberflächenenergie eines festen Körpers (Zusatz), *Z. Phys. Chem.* **1909,** *65,* 545-548.

(27) Kirkland, A. I.; Jefferson, D. A.; Duff, D. G.; Edward, P. P.; Gameson, I.; Johnson, B. F. G.; Smith, D. J. Structural Studies of Trigonal Lamellar Particles of Gold and Silver. *The Royal Society* **1993**, *440*, 589-609.

(28) Nix, F. C.; MacNair, D. The Thermal Expansion of Pure Metals: Copper, Gold, Aluminum, Nickel, and Iron. *Phys. Rev.* **1941**, *60*, 597–605.

(29) Boswell, F. W. C. Precise Determination of Lattice Constants by Electron Diffraction and Variations in the Lattice Constants of Very Small Crystallites. *Proc. Phys. Soc. Sect. A* **1954**, *64*, 465–476.

(30) Varns, R.; Strange, P. Stability of Gold Atoms and Dimers Adsorbed on Graphene. *J. Phys. Condens. Matter* **2008**, *20*, 225005, 1-8.

(31) Wang, H.; Feng, Q.; Cheng, Y.; Yao, Y.; Wang, Q.; Li, K.; Schwingenschlögl, U.; Zhang, X. X.; Yang, W. Atomic Bonding between Metal and Graphene. *J. Phys. Chem. C* **2013**, *117*, 4632–4638.

(32) Wu, Y. A.; Fan, Y.; Speller, S.; Creeth, G. L.; Sadowski, J. T.; He, K.; Robertson, A. W.; Allen, C. S.; Warner, J. H. Large Single Crystals of Graphene on Melted Copper Using Chemical Vapor Deposition. *ACS Nano* **2012**, *6*, 5010–5017.

(33) Fan, Y.; He, K.; Tan, H.; Speller, S.; Warner, J. H. Crack-Free Growth and Transfer of Continuous Monolayer Graphene Grown on Melted Copper. *Chem. Mater.* **2014**, *26*, 4984–4991.